

Supplementary Information

for

Molten α -H₃PO₄: A New Electrolyte for the Anodic Synthesis of Self-Organized Oxide Structures – WO₃ Nanochannel Layers and Others

Marco Altomare,[†] Ole Pfoch,[†] Alexei Tighineanu,[†] Robin Kirchgeorg,[†] Kiyoungh Lee,[†] Elena Selli,[§] and Patrik Schmuki^{*,†,‡}

[†]Department of Materials Science, Institute for Surface Science and Corrosion WW4-LKO, Friedrich-Alexander University, Martensstraße 7, D-91058 Erlangen, Germany

[‡]Chemistry Department, Faculty of Sciences, King Abdulaziz University, 80203 Jeddah, Saudi Arabia Kingdom

[§]Department of Chemistry, University of Milano, Via C. Golgi 19, I-20133 Milan, Italy

Corresponding Author ^{*}schmuki@ww.uni-erlangen.de

CONTENTS

Growth of anodic WO ₃ layers on W foil	3
Growth of anodic WO ₃ layers on non-conductive glass.....	3
Characterization of anodic WO ₃ layers	4
Fabrication of gas-sensors	5
Gas-sensing experiments	6
Table S1 – Preliminary experiments in pure <i>o</i> -H ₃ PO ₄	7
Table S2 – Preliminary experiments in <i>o</i> -H ₃ PO ₄ -based electrolytes.....	8
Table S3 – Preliminary experiments in other P-containing acids.....	9
Fig. S1 – TEM analysis	10
Fig. S2 – Effect of electrolyte temperature.....	10
Fig. S3 – J-time profiles	11
Fig. S4 – Karl Fischer analysis (water content determination)	12
Fig. S5 – XRD analysis – WO ₃ films on glass slides	12
Fig. S6 – XRD analysis – WO ₃ films on W foils and on quartz slides	13
Fig. S7 – Effect of annealing temperature	14
Fig. S8 – XPS analysis	15
Fig. S9 – EDX analysis.....	16
Fig. S10 – Anodization in pyro- and poly-phosphoric acid.....	16
Fig. S11 – Gas-sensor fabrication.....	17
Fig. S12 – W and WO ₃ films on glass	18
Fig. S13 – Gas-sensing device.....	18
Scheme S1 – Gas-sensing setup	19
Fig. S14 – Gas-sensing results.....	19
Fig. S15 – PEC water splitting	21
References.....	22

Growth of anodic WO₃ layers on W foil

Preliminary anodization experiments were carried out on W foils in order to optimize the experimental conditions, that is, to obtain high aspect ratio WO₃ films with vertically aligned nanochannels. The results of preliminary anodization experiments are summarized in Tables S1-S3.

For these experiments, W foils (0.125 mm thick, 99.95% purity, Advent Research Materials LTD, Oxford, UK) were cut into 1 cm x 2 cm pieces, cleaned by ultra-sonication in acetone, ethanol and de-ionized water (10 min each) and finally dried in a N₂ stream.

For growing WO₃ nanochannels, the anodization experiments were carried out in a two-electrode electrochemical cell where the W film and Pt foil were the working and the counter electrodes, respectively. The two electrodes were immersed into the electrolyte in vertical configuration and placed at a distance of 2 cm from each other. The electrolyte was constantly stirred and kept at the desired temperature by thermostatic control provided by a heating-stirring plate. The heating plate was equipped with a thermocouple that was fully wrapped into a Teflon tape and immersed into the anodizing electrolyte. The experiments were performed under potentiostatic conditions, that is, by applying a constant direct current potential of 1-60 V (no sweeping) provided by a Volcraft VLP 2403 Pro power source. The resulting current density was recorded by using a Keithley 2100 6 ½ Digit multimeter interfaced with a laptop.

In most of the experiments, the electrolyte was composed of pure molten ortho-phosphoric acid (*o*-H₃PO₄, ≥ 99 %, Sigma-Aldrich). However, during preliminary anodization, a few additives were also added to the electrolyte. Precisely, DI H₂O (18.2 MΩ cm), Ethylene Glycol (Fluka Analytical, ≥ 99.5 %) and Glycerol (Sigma Aldrich, ≥ 99.5 %) were used as additives for the *o*-H₃PO₄-based electrolytes. Also pyrophosphoric acid (H₄P₂O₇, ≥ 90 %, Fluka Analytical) and polyphosphoric acid (115 %, Sigma-Aldrich) were used (as received, *i.e.*, pure) as anodizing media (see Fig. S10).

Growth of anodic WO₃ layers on non-conductive glass

W layers (600-700 nm-thick, see Fig. S12) were deposited by e-beam evaporation (PLS 500 Labor System, Balzers-Peiffer, Germany) on non-conductive glass substrates at a pressure of 1-6 x 10⁻⁶

mbar and with a deposition rate of 0.1 nm s^{-1} . Tungsten granules (2-4 mm, 99.9 %, Chempur) were used as source of metal. Prior to evaporation, the glass substrates (7.5 cm x 2.5 cm microscope glass slides, VWR) were cut into 1.2 cm x 2.5 cm pieces, cleaned (in acetone, isopropanol and DI H_2O for 10 min each) and finally dried in a N_2 stream.

The W films on non-conductive glass were all anodized under optimized conditions, that is, in pure molten $o\text{-H}_3\text{PO}_4$ at 5 V and 100°C , in a two-electrode electrochemical cell as reported above. The anodization experiments were run long enough to anodize through the entire thickness of the W layer, *i.e.*, not to have a metallic W layer left beneath the anodic film – this was obtained when the current density significantly dropped (Fig. S11). By anodizing for *ca.* 4 h under such experimental conditions, *ca.* $1.3 \text{ }\mu\text{m}$ -thick transparent porous WO_3 layers were formed that exhibited excellent adhesion to the glass slide. These layers were used for fabricating the gas sensors. Such configuration of the device (see a sketch in Fig. S11) was adopted since preliminary experiments (WO_3 films on W foils or on FTO slides) showed the sensing measurements to be strongly affected by the presence of a conductive substrate. In particular, the response of devices fabricated on conductive substrates was relatively low, this because the current flowed preferentially through the conductive substrate, and changes in resistance of the anodic film upon exposure to analytes were relatively small.

Characterization of anodic WO_3 layers

A Hitachi field emission scanning electron microscope (FE-SEM S4800, Hitachi) was used for morphological characterization of the samples. The thickness of the anodic films was directly obtained from SEM cross-sectional micrographs. In the case of anodic WO_3 layers on W foils, the cross-sectional view was obtained by scratching off the anodic film with a blade. In the case of anodic WO_3 layers on non-conductive glass, the cross-sectional view was obtained either by scratching off the anodic film or by cracking the glass slides (for this, a diamond tip was used). Analysis of the morphological features of the WO_3 nanochannel structures (see Fig. 1-4 in main text) was performed by using the software Image J (data were then processed by Gaussian fitting).

Energy-dispersive X-ray spectroscopy (EDAX Genesis, fitted to SEM chamber) was also used for the chemical analysis.

Transmission electron microscopy (TEM) was performed by using a Philips CM300 UltraTWIN, equipped with a LaB6 filament and operated at 300 kV. TEM images and selective area diffraction (SAED) patterns were recorded with a fast scan (type F214) charge-coupled device camera from TVIPS (Tietz Video and Image Processing Systems), with an image size of 2048 x 2048 pixels. For TEM investigations, the samples were mechanically scratched from the substrate and the resulting powder was deposited on copper TEM grids coated with lacey carbon film.

X-ray diffraction (XRD) patterns were collected using an X'pert Philips PMD diffractometer with a Panalytical X'celerator detector, using graphite-monochromized Cu K α radiation ($\lambda = 1.54056 \text{ \AA}$).

Composition and chemical state of samples were determined by X-ray photoelectron spectroscopy (XPS) using a PHI 5600 Multi-Technique System (Physical Electronics, USA) equipped with a monochromatic Al K α X-ray source (1486.6 eV).

Fabrication of gas-sensors

As shown in Fig. S11, the fabrication of the gas-sensing devices was completed by annealing the porous WO₃ layers and by depositing Pt electrodes on their top.

XRD analysis showed that as-formed anodic films are typically amorphous (Fig. 5(a-b) in main text) and the gas-sensing experiments revealed that, along with Pt deposition onto the semiconductor (see below), the crystallization of the oxide is a key to fabricate functional gas-sensors (Fig. S14). Thus, the WO₃ films were annealed in air at different temperatures (250-650°C range) for 1 h, with a heating/cooling rate of 30 °C min⁻¹ by using a rapid thermal annealer (RTA, Jipelec JetFirst100).

Then, the anodic films were contacted on top by depositing two 200 nm-thick Pt electrodes through a mask by using a Leica EM SCD 500 plasma sputtering system (Fig. S13). The deposition was carried out at 16 mA and at a rate of 0.16-0.20 nm s⁻¹ (vacuum conditions, 10⁻² mbar of Ar).

Gas-sensing experiments

For the gas-sensing measurements, a device was placed into the sensing chamber (Scheme S1) and flushing with artificial air (Linde, Germany) was carried out until reaching a constant resistance measured by the device. The chamber was kept under thermostatic control by using a Eurotherm 3216-based temperature controller (Invensys Eurotherm, USA).

Gold wires were connected to the Pt electrodes that were sputter-deposited onto the annealed anodic WO₃ films. The resistance of the Pt/anodic film system was measured with a Keithley 2400 Source Meter (Keithley Instruments, USA) by applying a bias of 1 V. Preliminary experiments showed that the I-V characteristics of the WO₃ layers exhibited an ohmic response in this range of applied bias (not shown).

To investigate the device sensitivity, the Pt/WO₃ films were exposed to different concentrations of H₂. For this purpose, different amounts of H₂-Ar mixtures (90.000 ppm of H₂ in Ar, Linde, Germany) were injected into the background stream of artificial air. The flow of the different gases was controlled with MF1 (MKS Instruments, Germany) digital mass flow controllers. The relative response “*r*” and sensitivity “*s*” of the sensors were calculated according to following equation:

$$r = \frac{R_0 - R}{R_0} \cdot 100 \% \quad \text{Eq. (1)}$$

$$s = \frac{\delta(r)}{\delta(\text{H}_2 \text{conc.})} \quad \text{Eq. (2)}$$

where “*R*₀” and “*R*” are the resistance of the sensor when exposed to background air flow and to the H₂ injection, respectively.

Table S1 – Preliminary experiments in pure *o*-H₃PO₄

Anodization experiments carried out on W foils in pure molten *o*-H₃PO₄[§].

T (°C)	E (V)	TIME (h)	DESCRIPTION	THICKNESS
20	20	0.5	Little extent of etching	Not measured
	30			
	40		Large extent of etching	
20	5	1	Compact oxide layer	Few tens of nm
40				
60			Porous layer	Few tens of nm
80				
80	20	1	Channels with a little extent of etching at the top	400 – 500 nm
	40		Large extent of etching	Not measured
100	1	1	Porous layer	Few tens of nm
	2.5		Highly ordered nanochannels, smooth and flat at the top	300 nm
	5			400 – 600 nm
	5*			
	10			0.6 – 1.0 μm
	10	4		0.8 – 1.2 μm
	15	1	Nanochannels with a little extent of etching at the top	1.1 – 1.3 μm
	20		Porous layer	1.2 – 1.4 μm
100	5	0.5	Porous layer	150 – 200 nm
		2	Highly ordered nanochannels, smooth and flat at the top	600 – 700 nm
		4		1.3 – 1.5 μm
		8		1.9 – 2.1 μm
		12	Ordered nanochannels with nanograss [†] at the top	2.1 – 2.6 μm
		24		3.4 – 3.6 μm
		2.5		1.0 – 1.1 μm
120	5	1	Nanochannels with a little extent of etching at the top	400 – 500 nm
90	5	1	Highly ordered nanochannels, smooth and flat at the top	100 – 200 nm
95				200 nm
105				400 – 450 nm
110				1.0 – 1.1 μm
110*				800 – 900 nm
115			Ordered nanochannels with grass at the top	1.0 – 1.3 μm

[§] *o*-H₃PO₄ = ortho-phosphoric acid; solid at room temperature (melting point = 42.3°C).

*the electrolyte was aged by anodizing a W foil for 100 h at 2.5 V and 100°C.

*the electrolyte was aged by anodizing a W foil for 25 h at 5V and 110°C.

[†]the term “nanograss” refers to needle-like nanosized structures that form at the top of the anodic layer as consequence of considerable etching (typically observed for extended anodization experiments).

Table S2 – Preliminary experiments in *o*-H₃PO₄-based electrolytes

Anodization experiments carried out on W foils in *o*-H₃PO₄-based electrolytes.

ADDITIVE	T (°C)	E (V)	TIME (h)	DESCRIPTION	THICKNESS
H ₂ O traces*	110	5	1	Ordered nanochannels with grass at the top	1.0 – 1.1 μm
0.5vol.%H ₂ O [§]	100			Highly ordered nanochannels, smooth and flat at the top	300 – 400 nm
1vol.%H ₂ O [§]	20	5	0.5	Compact oxide layer	Not measured
		20		Little extent of etching	
		40			
2vol.%H ₂ O [§]	100	5	1	Highly ordered nanochannels, smooth and flat at the top	500 – 600 nm
		10		Channels with a little extent of etching at the top	
		15			
5vol.%H ₂ O [§]	20	5	0.5	Compact oxide layer	Not measured
		20		Little extent of etching	
		40			
		60			
10vol.%H ₂ O [§]	20	5	0.5	Compact oxide layer	Not measured
		20		Large extent of etching	
		40			
	100	5	1	Ordered nanochannels with grass at the top	0.9 – 1.1 μm
		10	0.5		0.6 – 1.1 μm
25vol.%EG [‡]	100	5	1	Highly ordered nanochannels, smooth and flat at the top	300 – 400 nm
		20	0.3	Large extent of etching	Not measured
25vol.%GLY [†]	50	10	1	Compact oxide layer	Not measured
	80	20		Porous layer	Few tens of nm
	100	10	0.3	Ordered nanochannels, smooth and flat at the top	300 – 400 nm

*the electrolyte was exposed overnight to ambient air to allow for moisture uptake and no preliminary heat treatment was performed before anodizing.

[§]the water content (in terms of vol.%) represents a nominal value, calculated by taking into account the volume of pure water added to the electrolyte, and by assuming the latter to be water-free (see Fig. S4 for more details on the electrolyte water content).

[‡]EG = Ethylene glycol.

[†]GLY = Glycerol.

Table S3 – Preliminary experiments in other P-containing acids

Anodization experiments carried out on W foils in other hot pure phosphorus-containing acid electrolytes.

ACID	T (°C)	E (V)	TIME (h)	DESCRIPTION	THICKNESS
H ₄ P ₂ O ₇ *	100	5	1	Porous layer	Few tens of nm
		20		Channels with a large extent of etching	250 – 300 nm
		40	0.3	Large extent of etching	Not measured
	110	5	1	Highly ordered nanochannels, smooth and flat at the top	1.0 – 1.1 μm
		10		Channels with a large extent of etching	450 – 550 nm
		20			
	120	5		Highly ordered nanochannels, smooth and flat at the top	1.1 – 1.2 μm
POLY‡	120	5	1	Ordered nanochannels, smooth and flat at the top	200 – 250 nm

*H₄P₂O₇ = pyrophosphoric acid; solid at room temperature (melting point = 71.5°C).

‡POLY = polyphosphoric acid; viscous liquid at room temperature.

Fig. S1 – TEM analysis

TEM images of as-formed WO_3 nanochannel layers grown by anodization of W in molten pure *o*- H_3PO_4 at 5 V and 100°C.

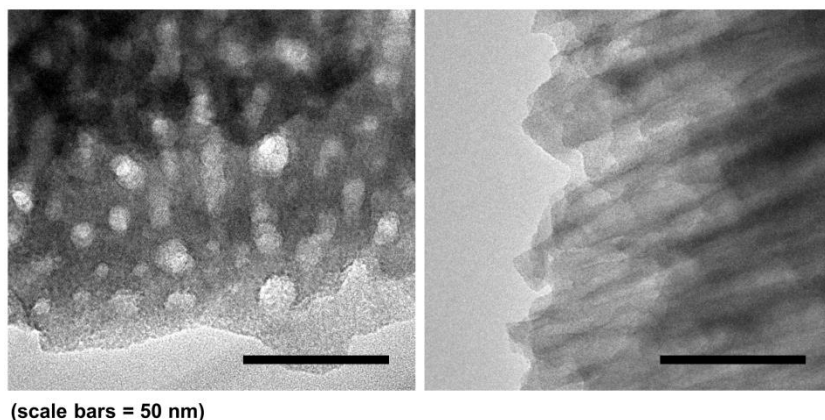


Fig. S2 – Effect of electrolyte temperature

SEM images of WO_3 films grown by anodization of W foils in pure molten *o*- H_3PO_4 at 5 V for 1 h, at different temperatures of the electrolyte (60-120°C). In the case of the anodic layer formed at 80°C, no clear cross sectional image could be taken (*i.e.*, a few nm-thick film).

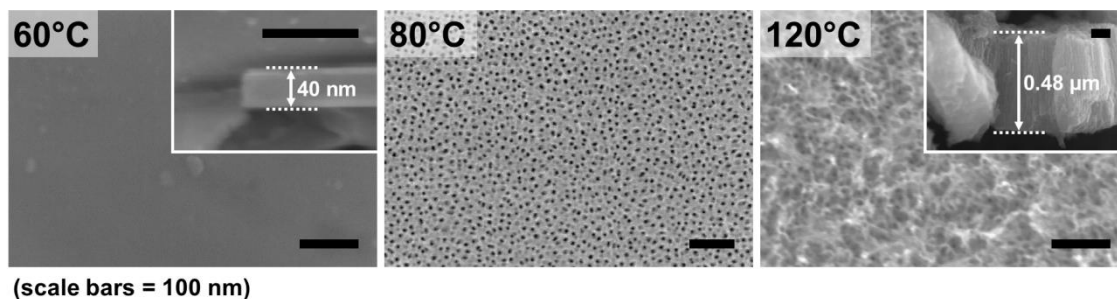
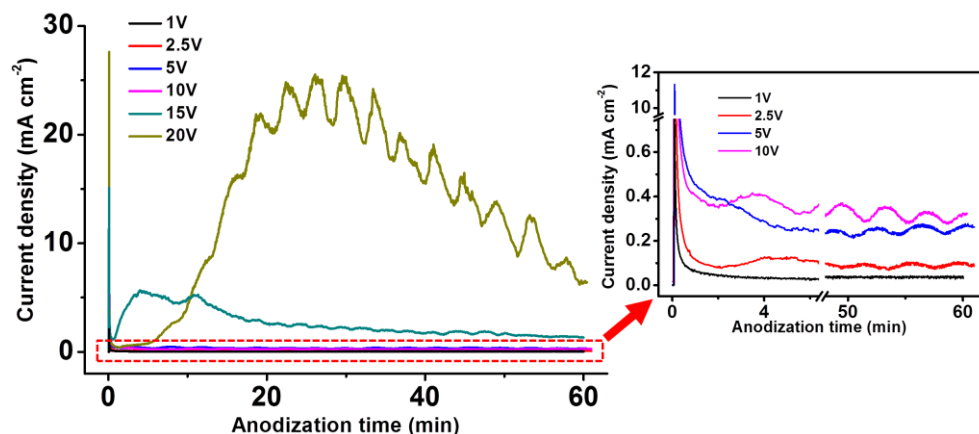


Fig. S3 – J-time profiles

Current density (J) vs. time profiles of anodization experiments carried out on W foils in molten pure o -H₃PO₄ at 100°C for 1 h, at different applied potential in the 1-20 V range (formed structures are shown in Fig. 2 in the main text).



The oscillation of the current density (visible also in the main text in Fig. 4, and in Fig. S11) is only an artifact given by the temperature feed-back control of the thermocouple. The latter is interfaced to the heating-stirring plate used for the anodization experiments, and allows for maintaining the electrolyte temperature at the desired value. However, slight control drifts take place, and the temperature of the molten o -H₃PO₄ typically oscillates by $\pm 3^\circ\text{C}$ (this may be also ascribed to the relatively high viscosity of the electrolyte which limits heat transfer). The current density measured during the anodization experiments mirrors such oscillating trend, being J strictly related to the electrolyte temperature.

Fig. S4 – Karl Fischer analysis (water content determination)

Water content (in ppm and %) of nominally pure α -H₃PO₄, molten and heated up to 60 and 100°C, determined by using a 756 KF Coloumeter (Metrohm).

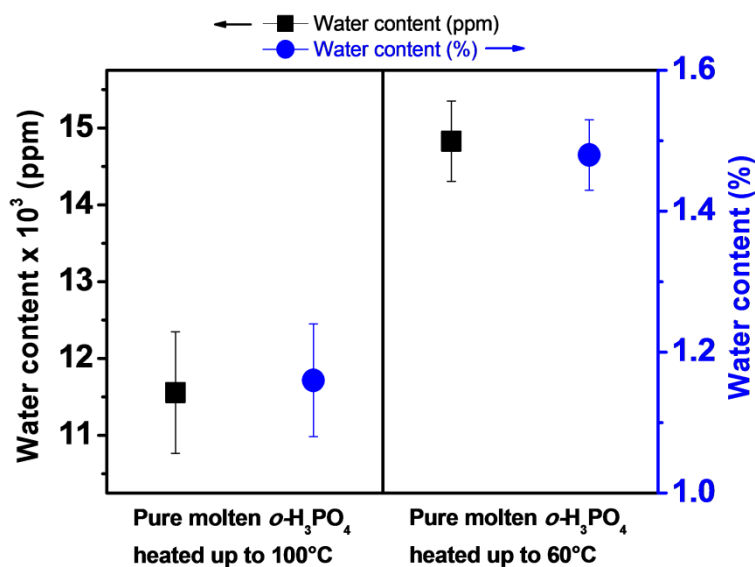
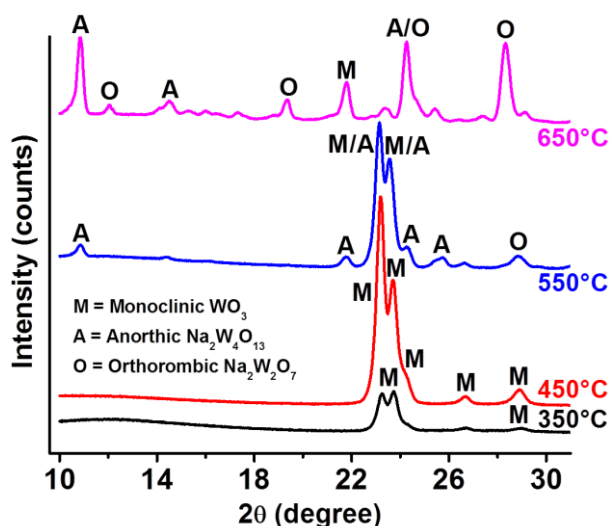


Fig. S5 – XRD analysis – WO₃ films on glass slides

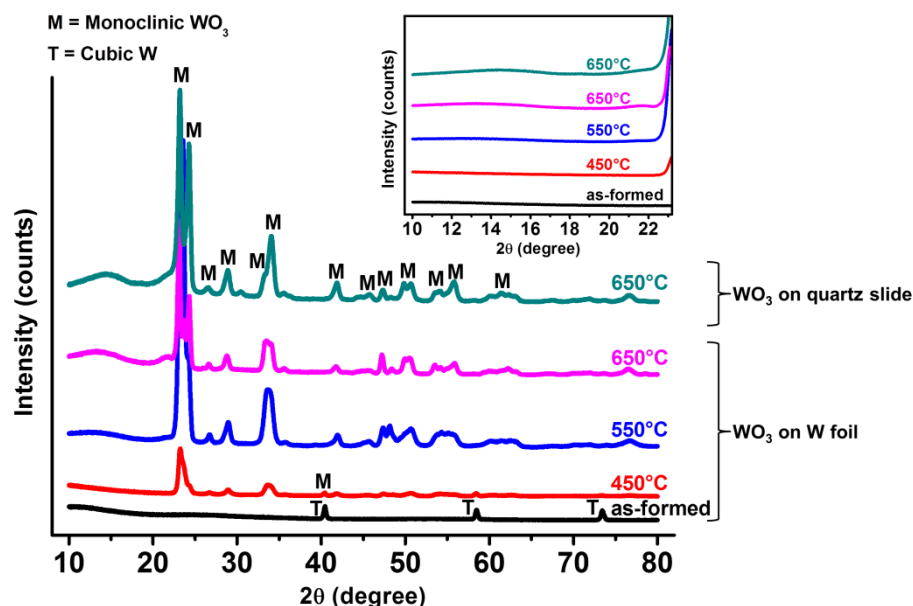
XRD patterns in the 10-30 degree region of WO₃ nanochannel layers grown by anodization of W in pure molten α -H₃PO₄ at 5 V and 100°C, and annealed at different temperatures in the 250-650°C range (air, 1 h).



WO₃ layers grown on glass slides were shown to convert also into various sodium tungstate species when crystallized at relatively high temperature (*e.g.*, $T \geq 550^\circ\text{C}$).

Fig. S6 – XRD analysis – WO₃ films on W foils and on quartz slides

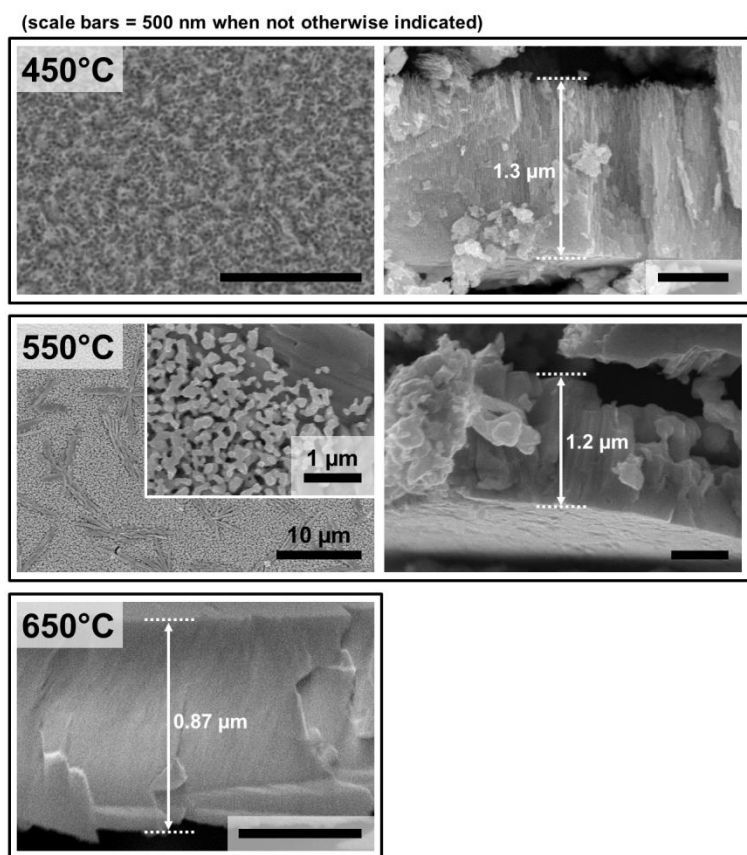
XRD patterns of as-formed and annealed WO₃ nanochannel layers grown by anodizing W foils and W films e-beam evaporated onto quartz slides. The anodization experiments were carried out in pure molten *o*-H₃PO₄ at 5 V and 100°C. The WO₃ layers were annealed at different temperatures in the 450-650°C range (air, 1 h). The inset shows the XRD patterns in the 10-22 degree region.



Conversely to WO₃ films grown on glass slides, the WO₃ nanochannel layers grown on W foils or on quartz slides were shown to convert into monoclinic phase only when annealed at $T \geq 450^\circ\text{C}$, and no formation of sodium tungstate species could be observed (compare the XRD patterns in the 10-22 degree region to data in Fig. S5, and see Fig. S8 for more discussion).

Fig. S7 – Effect of annealing temperature

SEM images of WO₃ nanochannel layers anodically grown on non-conductive glass substrate and annealed at different temperatures (450-650°C, in air, 1 h).

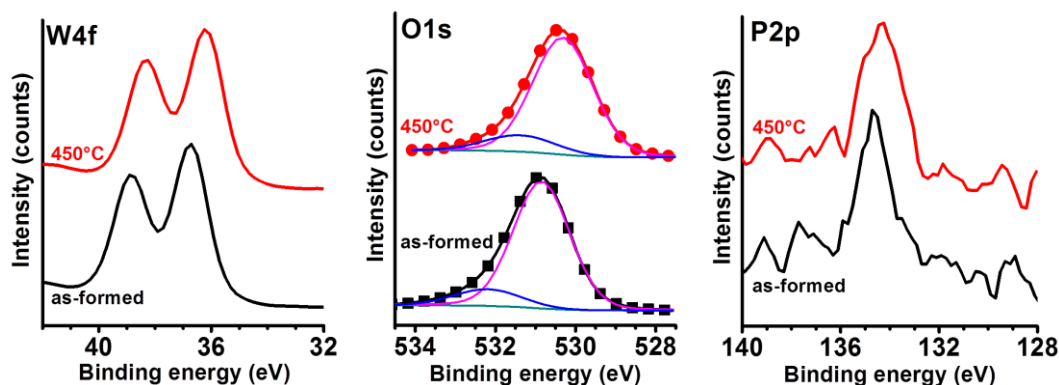


The nanochannel structures were shown to withstand thermal treatment at temperatures up to 450°C. On the contrary, high annealing temperatures ($\geq 550^\circ\text{C}$) led to significant sintering and collapse of the structures.

Besides the effect on the morphological features, relatively high annealing temperature ($\geq 550^\circ\text{C}$) led also to formation of sodium tungstate species (these with different stoichiometry and crystallographic features) as proved by appearance in the XRD patterns of intense reflections mainly at 10.8, 24.3 and 28.3 degree (see Fig. S5).¹ These results can be explained by assuming that at such annealing temperatures, solid state reaction occurs that leads to diffusion of Na ions from the glass substrate through the oxide film. This is in agreement with WO₃ crystallographic features and consequent ability to intercalate Na⁺ ions.²

Fig. S8 – XPS analysis

High resolution XPS spectra in the W4f, O1s and P2p regions of WO₃ nanochannel layers (as-formed and annealed at 450°C, air, 1 h) grown by anodization of W in pure molten *o*-H₃PO₄, at 5 V, 100°C.



The survey spectrum of the film annealed at 450°C (Fig. 5(d) in main text) shows the Na1s signal. As mentioned above (Fig. S5 and S7), one can explain this assuming that the thermal treatment at 450°C enables Na⁺ intercalation. On the other hand, the film annealed at this temperature was shown to be composed of monoclinic WO₃ (Fig. 5(a,c)). Thus we assume that only higher annealing temperatures ($\geq 550^\circ\text{C}$) enable intercalation of significant amounts of Na⁺ ions with consequent transformation of WO₃ into stoichiometric Na₂W₂O₇.

The high resolution XPS spectra show that after annealing at 450°C a *ca.* 0.5 eV-shift of the W4f doublet towards lower binding energies can be seen. According to the literature, a shift toward higher binding energies is typically observed after annealing, that is ascribed to complete oxidation of the anodic film to form stoichiometric WO₃ and also to a reduction of hydroxide species and water adsorbed at the oxide surface.³ Therefore, the shift towards lower binding energies can be due to intercalation of Na ions that induces partial reduction of WO₃ (in line with XRD and XPS data).

The O1s signals were deconvoluted into two peaks by Gaussian fitting: the main peaks at 530.88 and 530.28 eV are attributed to lattice oxygen and are in line with the literature on anodic WO₃.^{4,5} On the other hand, the peaks at higher binding energies, *i.e.*, at *ca.* 532.27-531.48 eV, are attributable to adsorbed hydroxide.^{4,5}

Fig. S9 – EDX analysis

EDX spectra and relative data for as-formed and annealed (450°C) WO₃ nanochannel layers that were anodically grown on W foils in pure molten *o*-H₃PO₄, at 5 V, 100°C. The peaks of aluminum are ascribed to the aluminum sample holder.

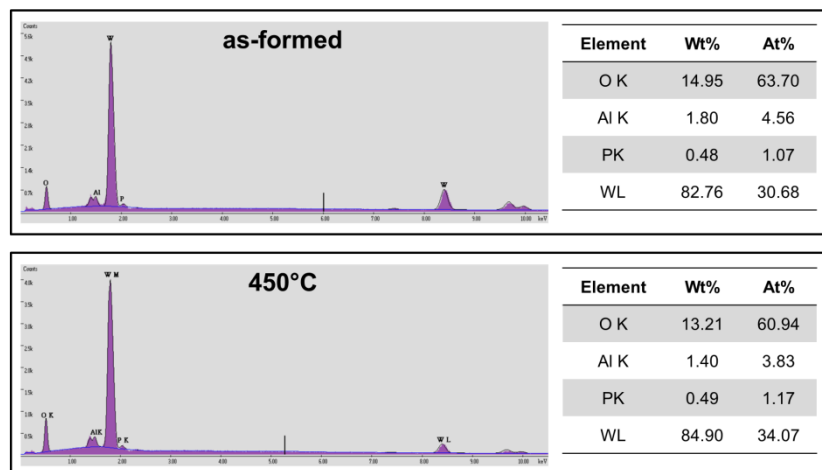
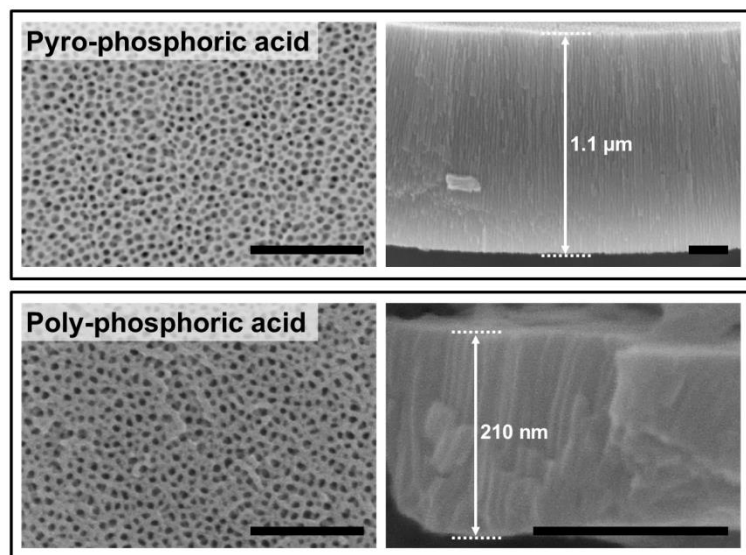


Fig. S10 – Anodization in pyro- and poly-phosphoric acid

SEM images of WO₃ nanochannel layers grown by anodizing W foils at 120°C (5 V, 1 h) in (nominally) pure pyro- and poly-phosphoric acid.



(scale bars = 200 nm)

Fig. S11 – Gas-sensor fabrication

(a) Sketch of the different steps for fabricating the gas-sensors; (b) J-time profile recorded during the fabrication of the WO_3 nanochannel layer on a non-conductive glass slide and optical pictures of the obtained porous transparent film; (c) Sketch of the resistive gas-sensor configuration adopted in this work, that is, with the anodic nanoporous WO_3 film grown on non-conductive glass, compared to an alternative configuration which implies the direct growth of the anodic layer on the W metal foil or, more generally, on a conductive substrate.

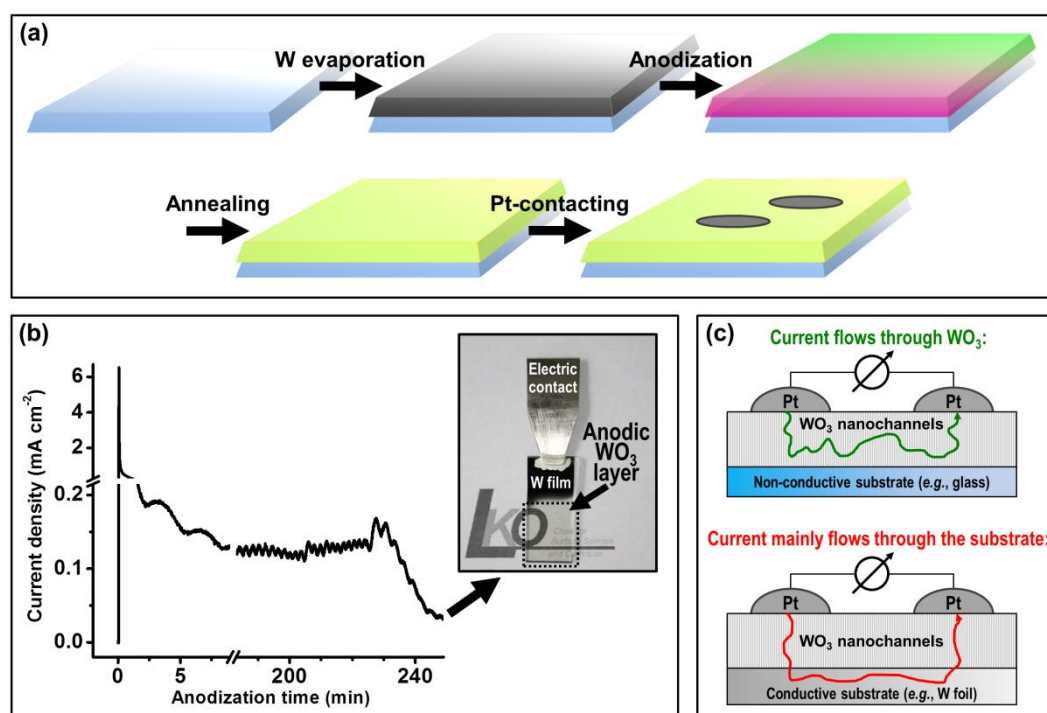


Fig. S12 – W and WO₃ films on glass

Top view and cross sectional SEM images of (a) 600 nm-thick W film evaporated onto non-conductive glass slide, and (b) 1.3 μm -thick WO₃ nanochannel layer formed by complete anodization (*ca.* 4 h) of the W film in pure molten *o*-H₃PO₄ at 5 V and 100°C. The volume expansion is ascribed to the lower density of the metal oxide compared to that of the metal.⁶

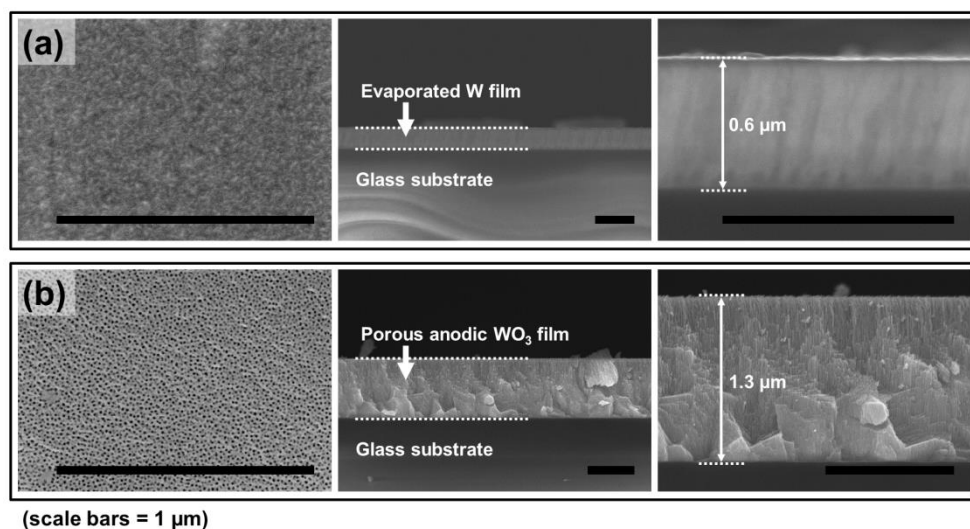
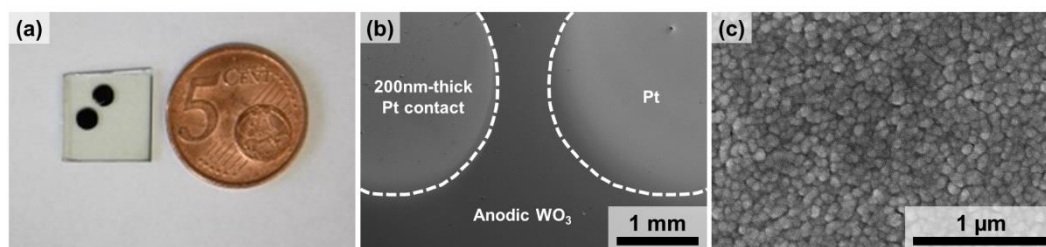


Fig. S13 – Gas-sensing device

(a) Optical and (b,c) top view SEM pictures of a gas-sensing device fabricated from WO₃ nanochannel layers anodically grown in pure molten *o*-H₃PO₄ (5 V, 100°C) on non-conductive glass substrates; (b) Low magnification SEM image of the device showing the anodic layer and the two sputtered Pt electrodes; (c) High magnification SEM image of the sputtered Pt electrode.



Scheme S1 – Gas-sensing setup

Sketch of the gas-sensing setup.

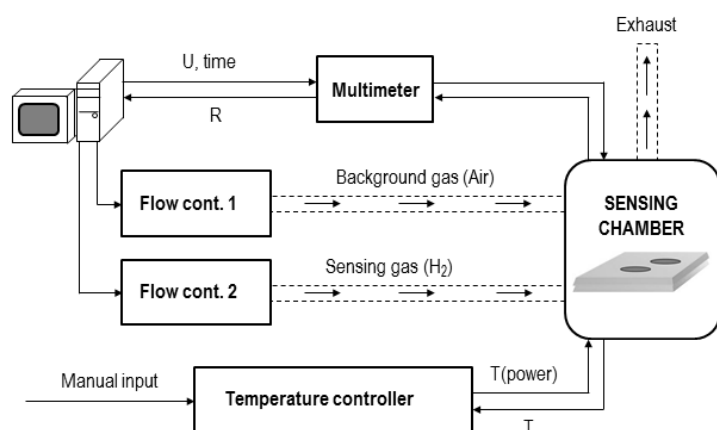
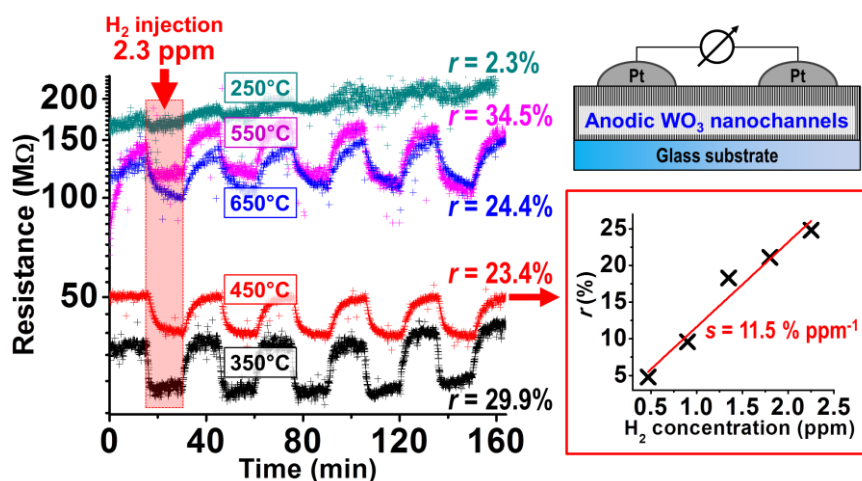


Fig. S14 – Gas-sensing results

H₂ sensing response of layers annealed at different temperatures (250-650°C) to H₂ injections of 2.3 ppm, at a sensing temperature of 120°C. Up-right: sketch of the gas-sensor; Inset: response of a sensor crystallized at 450°C to H₂ injections of different concentrations (500 ppb - 2.3 ppm) at a sensing temperature of 120°C.



Overall, the sensing results were well in line with the H₂ sensing mechanism reported in the literature.⁷⁻⁹ Briefly, the sensing ability of WO₃ is generally ascribed to reduction of sensor resistance upon exposure to H₂ (reducing gas). This occurs because H₂ is oxidized by the oxygen species adsorbed at the surface of the oxide, forming water as final product (“receptor” function).⁷ Thus, the consumption of adsorbed oxygen leads to the increase of conductivity of the sensor (“transducer” function). A similar effect can be brought about by most of the acidic gases (*e.g.*, H₂S,

NO_x, etc.). Also, Pt is typically deposited onto the WO₃ structures, this with a two-fold effect: *i*) it improves the sensitivity and reduces the response time of the sensors; and *ii*) it increases the selectivity of the device towards H₂, this because H₂ adsorption and consequent oxidation is particularly triggered by Pt deposits.¹⁰ More precisely, the increase of sensitivity occurs not only through a direct electronic interaction between Pt and the semiconductor surface (enabling a strong catalytic Schottky contact), but also by “spill-over effect”, which means that Pt remarkably facilitates the oxidation of H₂. This typically leads to injection, into the WO₃ conduction band, of larger amount of electrons upon exposure to H₂, and therefore to an enhanced response of the sensing device.¹⁰

A series of preliminary experiments showed the sensors to deliver a reliable signal at relatively low sensing temperature: stable and reproducible response as high as of *ca.* 23% to H₂ injections of 2.3 ppm was measured at 80-120°C.

Concerning the effect of thermal treatment on the sensing ability (Fig. 4 in the main text), devices annealed at relatively high temperatures ($\geq 550^\circ\text{C}$) delivered a slow drop and recovery of the resistance while films treated at 250°C showed poor response. These results correspond well with XRD and SEM analysis, that is, films annealed at temperature $\geq 550^\circ\text{C}$ underwent sintering (significant loss of porosity) and conversion into tungstate species (Fig. S5, S7 and S8), while structures treated at 250°C resulted not crystalline (Fig. 5(a) in the main text).

Instead, a proper annealing treatment at 350-450°C led the WO₃ channels to deliver the best response, in terms of both speed and magnitude, that is, a large and markedly fast resistance-drop and recovery upon exposure to H₂ pulses of a concentration as low as 2.3 ppm.

The gas-sensing ability of devices crystallized at 450°C was also assessed upon exposure to H₂ concentration in the 0.5-2.3 ppm range (Inset): the response to H₂ pulses of 500 ppb was of *ca.* 5% and the devices also showed, in this range of H₂ concentration, a linear correlation between the response and the analyte amount (sensitivity $s = 11.5 \text{ \% ppm}^{-1}$).

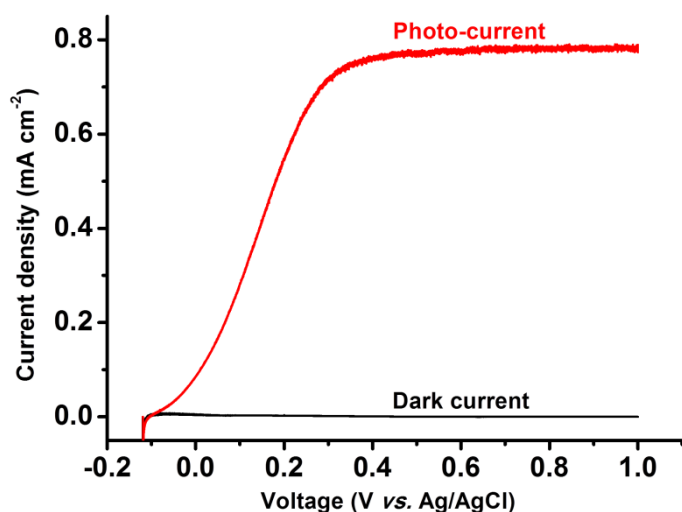
In comparison to previous literature reports on WO₃-based sensors (Pt- or Pd-decorated) showing reliable detection of H₂ only down to concentration of *ca.* 40 ppm at room temperature,¹¹ or down to

5 ppm at 250°C,¹² our Pt-contacted structures show a nearly two-order (80-times) and one-order of magnitude lower limit of detection, respectively.

Fig. S15 – PEC water splitting

Photo-electrochemical (PEC) water splitting results measured with WO₃ nanochannel layers grown by anodization of W foils in pure molten *o*-H₃PO₄ at 5 V and 100°C. The anodization experiments lasted 4 h and the layers thickness was of *ca.* 1-1.3 μm. Prior to the PEC measurements, the WO₃ layers were annealed at 450°C (air, 1 h) to convert the anodic structures into a monoclinic WO₃ phase.

The PEC water-splitting ability of the crystalline anodic films was investigated in aqueous 0.5 M Na₂SO₄ (containing also 0.1 M HCOONa), with a three-electrode configuration, consisting of a WO₃ photo-anode used as working electrode, a saturated Ag/AgCl electrode as reference and a platinum foil as counter electrode. An external bias, provided by a scanning potentiostat (Jaissle IMP 88 PC) with a scan rate of 1 mV s⁻¹, was applied to the PEC cell to record the photocurrent response (and also the dark current). The photocurrent density was calculated by dividing the photocurrent response (in mA) by the anodic oxide area (0.385 cm²) irradiated by the light source. The experiments were carried out under simulated AM 1.5 illumination provided by a solar simulator (300 W Xe lamp with a Solarlight optical filter) with an irradiation power of 100 mW cm⁻². The light intensity was measured prior to the experiments using a calibrated Si photodiode.



The crystalline *ca.* 1-1.3 μm -thick WO_3 nanochannel layers deliver a positive photo-current under solar light irradiation, and under anodic bias (relative to the flat-band potential). These results confirmed the n-type behavior of the anodic WO_3 structures.¹³

References

- (1) Okada, K.; Morikawa, H.; Marumo, F.; Iwai, S. *Acta Crystallogr. Sect. B Struct. Crystallogr. Cryst. Chem.* **1975**, *31*, 1200.
- (2) Zhang, J.; Benson, D.; Tracy, C. *J. Electrochem. Soc.* **1997**, *144*, 2022.
- (3) Nakagawa, H.; Yamamoto, N.; Okazaki, S.; Chinzei, T.; Asakura, S. *Sens. Actuators, B* **2003**, *93*, 468.
- (4) Leftheriotis, G.; Papaefthimiou, S.; Yianoulis, P.; Siokou, A. *Thin Solid Films* **2001**, *384*, 298.
- (5) Baek, Y.; Yong, K. *J. Phys. Chem. C* **2007**, *111*, 1213.
- (6) Yasuda, K.; Schmuki, P. *Electrochim. Acta* **2007**, *52*, 4053.
- (7) Shaver, P. *J. Appl. Phys. Lett.* **1967**, *11*, 255.
- (8) Xu, Z. *J. Vac. Sci. Technol. A* **1990**, *8*, 3634.
- (9) Smith, D. J.; Vatelino, J. F.; Falconer, R. S.; Wittman, E. L. *Sens. Actuators, B* **1993**, *13*, 264.
- (10) Yamazoe, N. *Sens. Actuators, B* **1991**, *5*, 7.
- (11) Kukkola, J.; Mäklin, J.; Halonen, N.; Kyllönen, T.; Tóth, G.; Szabó, M.; Shchukarev, A.; Mikkola, J.-P.; Jantunen, H.; Kordás, K. *Sens. Actuators, B* **2011**, *153*, 293.
- (12) Mozalev, A.; Calavia, R.; Vázquez, R. M.; Gràcia, I.; Cané, C.; Correig, X.; Vilanova, X.; Gispert-Guirado, F.; Hubálek, J.; Llobet, E. *Int. J. Hydrogen Energy* **2013**, *38*, 8011.
- (13) Hodes, G.; Cahen, D.; Manassen, J. *Nature* **1976**, *260*, 312.